

SVGA-Net: Sparse Voxel-Graph Attention Network for 3D Object Detection from Point Clouds

Qingdong He, Zhengning Wang*, Hao Zeng, Yi Zeng, Yijun Liu

University of Electronic Science and Technology of China

heqingdong@alu.uestc.edu.cn, zhengning.wang@uestc.edu.cn, {haozeng, zengyi, yijunliu}@std.uestc.edu.cn

Abstract

Accurate 3D object detection from point clouds has become a crucial component in autonomous driving. However, the volumetric representations and the projection methods in previous works fail to establish the relationships between the local point sets. In this paper, we propose Sparse Voxel-Graph Attention Network (SVGA-Net), a novel end-to-end trainable network which mainly contains voxel-graph module and sparse-to-dense regression module to achieve comparable 3D detection tasks from raw LIDAR data. Specifically, SVGA-Net constructs the local complete graph within each divided 3D spherical voxel and global KNN graph through all voxels. The local and global graphs serve as the attention mechanism to enhance the extracted features. In addition, the novel sparse-to-dense regression module enhances the 3D box estimation accuracy through feature maps aggregation at different levels. Experiments on KITTI detection benchmark and Waymo Open dataset demonstrate the efficiency of extending the graph representation to 3D object detection and the proposed SVGA-Net can achieve decent detection accuracy.

Introduction

With the widespread popularity of LIDAR sensors in autonomous driving (Geiger, Lenz, and Urtasun 2012) and augmented reality (Park, Lepetit, and Woo 2008), 3D object detection from point clouds has become a mainstream research direction. Compared to RGB images from video cameras, point clouds could provide accurate depth and geometric information (Yu et al. 2020) which can be used not only to locate the object, but also to describe the shape of the object (Zhang et al. 2020). However, the properties of unordered, sparsity and relevance of point clouds make it a challenging task to utilize point clouds for 3D object detection directly.

In recent years, several pioneering approaches have been proposed to tackle these challenges for 3D object detection on point clouds. The main ideas for processing point clouds data are to project point clouds to different views (Simon et al. 2019; Chen et al. 2017; Ku et al. 2018; Liang et al. 2018; Yang, Luo, and Urtasun 2018) or divide the point clouds into equally spaced voxels (Li 2017; Zhou and Tuzel

2018; Yan, Mao, and Li 2018). Then convolutional neural networks and mature 2D objection detection frameworks (Ren et al. 2015; Redmon et al. 2016) are applied to extract features. However, because projection alone cannot capture the object’s geometric information well, many methods (Chen et al. 2017; Wang and Jia 2019; Qi et al. 2018; Sindagi, Zhou, and Tuzel 2019) have to combine RGB images in the designed network. While the methods using only voxelization do not make good use of the properties of the point clouds and bring a huge computational burden (Liu et al. 2019) as resolution increases. Apart from converting point clouds into other formats, some works (Shi, Wang, and Li 2019; Yang et al. 2019) take Pointnets (Qi et al. 2017a,b) as backbone to process point clouds directly. Although Pointnets build a hierarchical network and use a symmetric function to maintain permutation invariance, they fail to construct the neighbour relationships between the grouped point sets.

Considering the properties of point clouds, we should notice the superiority of graphs in dealing with the irregular data. In fact, in the domain of point clouds for segmentation and classification tasks, the method of processing with graphs has been deeply studied by many works (Qi et al. 2017; Bi et al. 2019; Landrieu and Simonovsky 2018; Shen et al. 2018; Wang et al. 2019). However, few researches have used graphs to make 3D object detection from point clouds. To our knowledge, Point-GNN (Shi and Rajkumar 2020) may be the first to prove the potential of using the graph neural network as a new approach for 3D object detection. Point-GNN introduces auto-registration mechanism to reduce translation variance and designs box merging and scoring operation to combine detection results from multiple vertices accurately. However, similar to ShapeContextNet (Xie et al. 2018) and Pointnet++ (Qi et al. 2017b), the relationship between point sets is not well established in the feature extraction process and a large number of matrix operations will bring heavy calculation burden and memory cost.

In this paper, we propose the sparse voxel-graph attention network (SVGA-Net) for 3D object detection. SVGA-Net is an end-to-end trainable network which takes raw point clouds as input and outputs the category and bounding boxes information of the object. Specifically, SVGA-Net mainly consists of voxel-graph network module and sparse-to-dense regression module. Instead of normalized rectangle voxels,

*Corresponding Author

Copyright © 2022, Association for the Advancement of Artificial Intelligence (www.aaai.org). All rights reserved.

we divide the point clouds into 3D spherical space with a fixed radius. The voxel-graph network aims to construct local complete graph for each voxel and global KNN graph for all voxels. The local and global serve as the attention mechanism that can provide a parameter supervision factor for the feature vector of each point. In this way, the local aggregated features can be combined with the global point-wise features. Then we design the sparse-to-dense regression module to predict the category and 3D bounding box by processing the features at different scales. Evaluations on KITTI benchmark and Waymo Open dataset demonstrate that our proposed method can achieve comparable results with the state-of-the-art approaches.

Our key contributions can be summarized as follows:

- We propose a new end-to-end trainable 3D object detection network from point clouds which uses graph representations without converting to other formats.
- We design a voxel-graph network, which constructs the local complete graph within each spherical voxel and the global KNN graph through all voxels to learn the discriminative feature representation simultaneously.
- We propose a novel 3D boxes estimation method that aggregates features at different scales to achieve higher 3D localization accuracy.
- Our proposed SVGA-Net achieves decent experimental results on the challenging KITTI 3D detection dataset and Waymo Open dataset.

Related work

Projection-based methods for point clouds. To align with RGB images, series of works process point clouds through projection (Chen et al. 2017; Ku et al. 2018; Liang et al. 2019). Among them, MV3D (Chen et al. 2017) projects point clouds to bird view and trains a Region Proposal Network (RPN) to generate positive proposals. It extracts features from LiDAR bird view, LiDAR front view and RGB image, for every proposal to generate refined 3D bounding boxes. AVOD (Ku et al. 2018) improves MV3D by fusing image and bird view features and merges features from multiple views in the RPN phase to generate positive proposals. Note that accurate geometric information may be lost in the high-level layers with this scheme.

Volumetric methods for point clouds. Another typical method for processing point clouds is voxelization. VoxelNet (Zhou and Tuzel 2018) is the first network to process point clouds with voxelization, which use stacked VFE layers to extract features tensors. Following it, a large number of methods (Liu et al. 2020; Yan, Mao, and Li 2018; Shi et al. 2020; Chen et al. 2019) divide the 3D space into regular grids and group the points in a grid as a whole. However, they often need to stack heavy 3D CNN layers to realize geometric pose inference which bring large computation.

Pointnet-based methods for point clouds. To process point clouds directly, PointNet (Qi et al. 2017a) and PointNet++ (Qi et al. 2017b) are the two groundbreaking works to design parallel MLPs to extract features from the raw irregular data, which improve the accuracy greatly. Taking them as backbone, many works (Shi, Wang, and Li 2019;

Qi et al. 2018; Lang et al. 2019; Yang et al. 2019, 2020) begin to design different feature extractors to achieve better performance. Although Pointnets are effective to abstract features, they still suffer feature loss between the local and global point sets.

Graph-based methods for point clouds. Constructing graphs to learn the order-invariant representation of the irregular point clouds data has been explored in classification and segmentation tasks (Kaul, Pears, and Manandhar 2019; Wang et al. 2019). Graph convolution operation is efficient to compute features between points. DGCNN (Wang et al. 2019) proposes EdgeConv in the neighbor point sets to fuse local features in a KNN graph. SAWNet (Kaul, Pears, and Manandhar 2019) extends the ideas of PointNet and DGCNN to learn both local and global information for points. Surprisingly, few researches have considered applying graph for 3D object detection. Point-GNN may be the first work to design a GNN for 3D object detection. Point-GNN (Shi and Rajkumar 2020) designs a one-stage graph neural network to predict the category and shape of the object with an auto-registration mechanism, merging and scoring operation, which demonstrate the potential of using the graph neural network as a new approach for 3D object detection.

Proposed method

In this section, we detail the architecture of the proposed SVGA-Net for 3D detection from point clouds. As shown in Figure 1, our SVGA-Net architecture mainly consists of two modules: voxel-graph network and sparse-to-dense regression.

Voxel-graph network architecture

Spherical voxel grouping. Consider the original point clouds are represented as $G = \{V, D\}$, where $V = \{p_1, p_2, \dots, p_n\}$ indicating n points in a D dimensional metric space. In our practice, D is set to 4 so each point in 3D space is defined as $v_i = [x_i, y_i, z_i]$, where x_i, y_i, z_i denote the coordinate values of each point along the axes X, Y, Z and the fourth dimension is the laser reflection intensity which denoted as s_i .

Then in order to cover the entire point set better, we use the iterative farthest point sampling (Qi et al. 2017b) to choose N farthest points $P = \{p_i = [v_i, s_i]^T \in R^4\}_{i=1,2,\dots,N}$. According to each point in P , we search its nearest neighbor within a fixed radius r to form a local voxel sphere:

$$h_i = \{p_1, p_2, \dots, p_i, \dots, p_j, \dots \mid \|v_i - v_j\|_2 < r\} \quad (1)$$

In this way, we can subdivide the 3D space into N 3D spherical voxels $H = \{h_1, h_2, \dots, h_N\}$.

Local point-wise feature. As shown in Figure 1, for each spherical voxel $h_i = \{p_j = [x_j, y_j, z_j, s_j]^T\}_{j=1,2,\dots,t}$ with t points (t varies for different voxel sphere), the coordinate information of all points inside form the input vector. We extract the local point-wise features for each voxel sphere by learning a mapping:

$$f(h_i) = MLP(p_j)_{j=1,2,\dots,t} \quad (2)$$

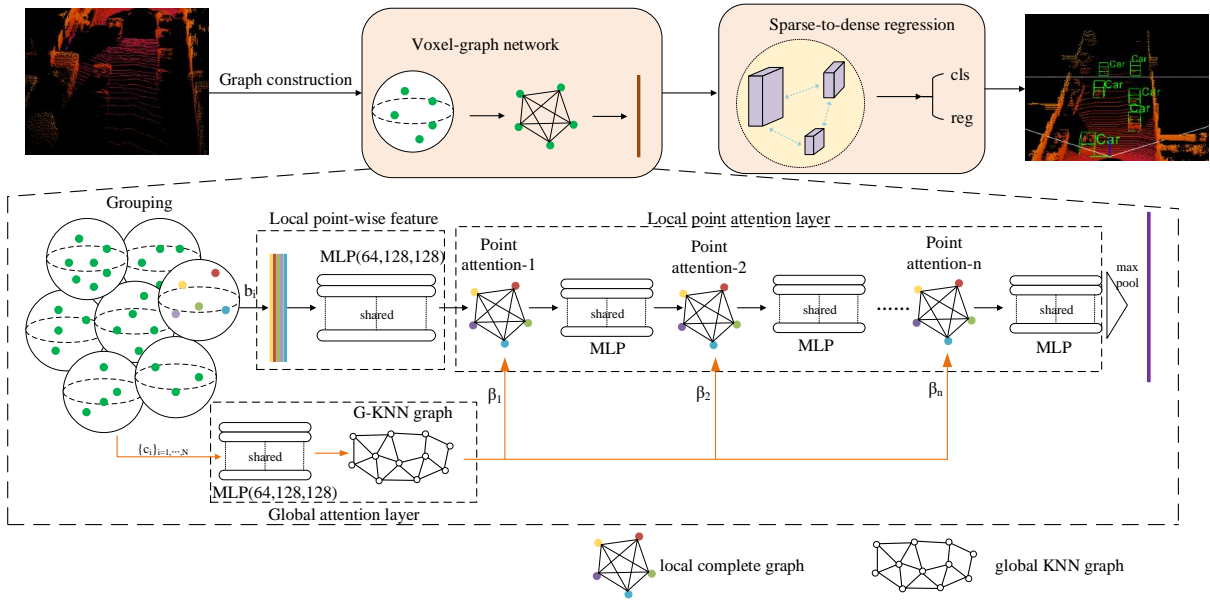


Figure 1: Architecture of the proposed SVGA-Net. The voxel-graph network takes raw point clouds as input, partitions the space into spherical voxels, transforms the points in each sphere to a vector representing the feature information. The sparse-to-dense regression module takes the aggregated features as input as generates the final boxes information.

Then, we could obtain the local point-wise feature representation for each voxel sphere $F = \{f_i, i = 1, \dots, N\}$, which are transformed by the subsequent layers for deeper feature learning.

Local point-attention layer. Taken the features of each nodes as input, the local point-attention layer outputs the refined features $F' = \{f'_i, i = 1, \dots, N\}$ through series of information aggregation. As shown in Figure 2, we construct a complete graph for each local node set and KNN graph for all the spherical voxels. We aggregate the information of each node according to the local and global attention score. The feature aggregation of j -th node is represented as:

$$f'_j = \beta_m \cdot f_j + \sum_{k \in \sqcup(p_j)} \alpha_{j,k} \cdot f_{j,k} \quad (3)$$

where f'_j denotes the dynamic updated feature of node p_j and f_j is the input feature of node p_j . $\sqcup(p_j)$ denotes the index of the other nodes inside the same sphere. $f_{j,k}$ denotes the feature of the k -th nodes inside the same sphere. $\alpha_{j,k}$ is the local attention score between node p_j and the other nodes inside the same sphere. β_m is the global attention score from the global KNN graph in the m -th iterations.

As shown in Figure 2 (a), we construct a complete graph for all nodes within a voxel sphere to learn the features constrained by each other. In order to allow each point to attend on every other point and make coefficients easily comparable across different points, we normalize them across all choices using the softmax function, so the local attention score $\alpha_{j,k}$ is calculated by:

$$\alpha_{j,k} = \text{softmax}_j(f_j, f_{j,k}) = \frac{\exp(f_j^T \cdot f_{j,k})}{\sum_{k \in \sqcup(p_j)} \exp(f_j^T \cdot f_{j,k})} \quad (4)$$

Global attention layer. By constructing the local complete graph, the aggregated features can only describe the local feature and do not integrate with the global information. So we design the global attention layer to learn the global feature of each spherical voxel and offer a feature factor aligned to each node.

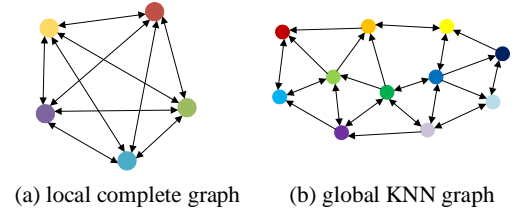


Figure 2: Graph construction. Each node with different color indicates the aggregated feature and arrows direction represents the information propagation direction with independent attention calculations scores. (a) local complete graph: for each node, we aggregate the information of all the nodes within the same spherical voxel according to the attention score. (b) global 3-NN graph: we aggregate the information of the three nearest neighbours around each node according to the attention score.

For the points within each h_i in N 3D spherical voxels $H = \{h_1, h_2, \dots, h_N\}$, we calculate the physical centers of all voxels which are denoted as $\{c_i\}_{i=1, \dots, N}$. Each center is learned by a 3-layer MLP to get the initial global feature $F_g = \{f_{g,1}, f_{g,2}, \dots, f_{g,N}\}$. As Figure 2 (b) shows, we construct a KNN graph for the N voxel sphere. For each node $f_{g,i}$, the attention score between node $f_{g,i}$ and its l -th neigh-

bor is calculated as follows:

$$\beta_{m,i} = \frac{f_{g,i}^T \cdot f_{g,i,l}}{\sum_{l \in \varpi(f_{g,i})} f_{g,i}^T \cdot f_{g,i,l}} \quad (5)$$

where $\varpi(f_{g,i})$ denotes the index of the neighbors of node $f_{g,i}$. m is the number of the point attention layers. Eq. 5 can be regarded as a weighted summation of the K neighbor nodes around a node, which guarantees the permutation invariance to the node order. And the final β_m is the average of K neighbors.

Voxel-graph features representation. The point attention operation on each spherical voxel can combine the parameter factor from both local and global, each of which is inserted with a 2-layer MLP with a nonlinear activation to transform each updated feature f'_j . By stacking multiple point attention layers, both local aggregated feature and global point-wise feature can be learned. We then apply maxpool on the aggregated feature to obtain the final feature vector.

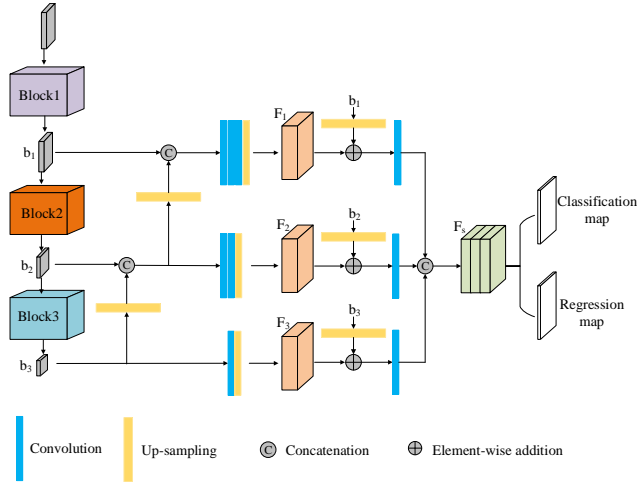


Figure 3: The architecture of the sparse-to-dense regression module. Features from the voxel-graph network are processed by series of region proposal extraction operations to generate the final classification and regression maps.

Sparse-to-dense regression

To process all the spherical voxel, we obtain a set of voxel sphere features, each of which corresponds to the spatial coordinates of the voxels and is taken as input of the sparse-to-dense regression module.

For each 3D bounding box in 3D space, the predicted box information is represented as $(x, y, z, l, w, h, \theta)$, where (x, y, z) is the center coordinate of the bounding box, (l, w, h) is the size information alongside length, width and height respectively, and θ is the heading angle. Feature map from the voxel-graph network is processed by region proposal regression module. The architecture of the specified sparse-to-dense regression (SDR) module is illustrated in Figure 3.

SDR module first apply three similar blocks as (Zhou and Tuzel 2018; Lang et al. 2019) to generate smaller the spatial resolution from top to down. Each block consist of series of $\text{Conv}(f_{in}, f_{out}, k, s, p)$ layers, followed by BatchNorm and a ReLU, where f_{in} and f_{out} are the number of input and output channels, k, s, p represent the kernel size, stride size and padding size respectively. The stride size is set to 2 for the first layer of each block to downsample the feature map by half, followed by sequence of convolutions with stride 1. And the output of the three blocks is denoted as b_1, b_2, b_3 respectively.

In order to combine high-resolution features with large receptive fields and low-resolution features with small receptive fields, we concatenate the output of the second and third modules b_2, b_3 with the output of the first and second modules b_1, b_2 after upsampling. In this way, the dense feature range of the lower level can be well combined with the sparse feature range of the higher level. Then a series of convolution operations with an upsampling layer are performed in parallel on three scale channels to generate three feature maps with the same scale size, which are denoted as F_1, F_2, F_3 .

In addition, we consider that the features output of F_1, F_2, F_3 are more densely fit to our final goal than the original three modules. Therefore, in order to combine the original sparse feature map and the series of processed dense feature maps, we combine the original output b_1, b_2, b_3 after upsampling and F_1, F_2, F_3 by element-wise addition. The final output F_s is obtained by concatenating the fused feature maps after a 3×3 convolution layer. And F_s is taken as input to perform category classification and 3D bounding box regression.

Loss function

We use a multi-task loss to train our network. Each prior anchor and ground truth bounding box are parameterized as $(x_a, y_a, z_a, l_a, w_a, h_a, \theta_a)$ and $(x_{gt}, y_{gt}, z_{gt}, l_{gt}, w_{gt}, h_{gt}, \theta_{gt})$ respectively. The regression residuals between anchors and ground truth are computed as:

$$\begin{aligned} \Delta x &= \frac{x_{gt} - x_a}{d_a}, \Delta y = \frac{y_{gt} - y_a}{d_a}, \Delta z = \frac{z_{gt} - z_a}{h_a} \\ \Delta w &= \log\left(\frac{w_{gt}}{w_a}\right), \Delta l = \log\left(\frac{l_{gt}}{l_a}\right), \Delta h = \log\left(\frac{h_{gt}}{h_a}\right) \\ \Delta \theta &= \sin(\theta_{gt} - \theta_a) \end{aligned} \quad (6)$$

where $d_a = \sqrt{(w_a)^2 + (l_a)^2}$. And we use Smooth L1 loss (Girshick 2015) as our 3D bounding box regression loss L_{reg} .

For the object classification loss, we apply the classification binary cross entropy loss.

$$L_{cls} = \gamma_1 \frac{1}{N_{pos}} \sum_i L_{cls}(p_i^{pos}, 1) + \gamma_2 \frac{1}{N_{neg}} \sum_i L_{cls}(p_i^{neg}, 0). \quad (7)$$

where N_{pos} and N_{neg} are the number of the positive and negative anchors. p_i^{pos} and p_i^{neg} are the softmax output for positive and negative anchors respectively. γ_1 and γ_2 are

positive constants to balance the different anchors, which are set to 1.5 and 1 respectively in our practice.

Our total loss is composed of two parts, the classification loss L_{cls} and the bounding box regression loss L_{reg} as:

$$L_{total} = \alpha L_{cls} + \beta \frac{1}{N_{pos}} \sum_{t \in \{x, y, z, l, w, h, \theta\}} L_{seg}(\Delta t^*, \Delta t). \quad (8)$$

where Δt^* and Δt are the predicated residual and the regression target respectively. Weighting parameters α and β are used to balance the relative importance of different parts, and their values are set to 1 and 2 respectively.

Experiments

KITTI. We first evaluate our method on the widely used KITTI 3D object detection benchmark (Geiger, Lenz, and Urtasun 2012). It includes 7481 training samples and 7518 test samples with three categories: car, pedestrian and cyclist. For each category, detection results are evaluated based on three levels of difficulty: easy, moderate and hard. Furthermore, we divide the training data into a training set (3712 images and point clouds) and a validation set (3769 images and point clouds) at a ratio of about 1: 1 (Ablation studies are conducted on this split). We train our model on train split and compare our results with state-of-the-art methods on both val split and test split. For evaluation, the average precision (AP) metric is to compare with different methods and the 3D IoU of car, cyclist, and pedestrian are 0.7, 0.5, and 0.5 respectively.

Waymo Open dataset. The Waymo Open Data Set (Sun et al. 2020) is by far the largest public data set for autonomous driving. There are a total of 1,000 sequences in the dataset. The training set contains 798 sequences with approximately 158000 point cloud samples, and the validation set contains 202 sequences with approximately 40000 point cloud samples. Different from KITTI, which only provides annotations in the camera’s FOV, Waymo Open Dataset provides annotations for objects throughout 360 degree. We evaluate our network on this large-scale dataset to further validate the effectiveness of our proposed method. We adopt the official released evaluation tools for evaluating our method, where the mean average precision (mAP) and the mean average precision weighted by heading (mAPH) are used for evaluation. The rotated IoU threshold is set as 0.7 for vehicle detection.

Training

Network Architecture. As shown in Figure 1, in the local point-wise feature and global attention layer, the point sets are first processed by 3-layer MLP and the sizes are all (64, 128, 128). In the local point attention layer, we stack $n = 3$ local point-attention graph to aggregate the features, each followed by a 2-layer MLP. And the sizes of the three MLPs are (128, 128), (128, 256) and (512, 1024) respectively. Following (Ku et al. 2018; Zhou and Tuzel 2018; Yang et al. 2019), we train two networks, one for cars and another for both pedestrians and cyclists.

For cars, we sample $N = 1024$ to form the initial point sets. To construct the local complete graph, we choose $r =$

1.8m. For anchors, an anchor is considered as positive if it has the highest IoU with a ground truth or its IoU score is over 0.6. An anchor is considered as negative if the IoU with all ground truth boxes is less than 0.45. To reduce redundancy, we apply IoU threshold of 0.7 for NMS. For cyclist and pedestrian, the number of the initial point sets is $n = 512$. We set $r = 0.8$ to construct the local graph. The anchor is considered as positive if its highest IoU score with a ground truth box or an IoU score is over than 0.5. And an anchor is considered as negative if its IoU score with ground truth box is less than 0.35. The IoU threshold of NMS is set to 0.6.

The network is trained in an end-to-end manner on GTX 1080 GPU. The ADAM optimizer (Kingma and Ba 2014) is employed to train our network and its initial learning rate is 0.001 for the first 140 epoches and is decayed by 10 times in every 20 epoches. We train our network for 200 epoches with a batch size of 16 on 4 GPU cards. Furthermore, we also apply data augmentation as (Lang et al. 2019; Zhou and Tuzel 2018) do to prevent overfitting.

Comparing with state-of-the-art methods

Performance on KITTI test dataset. We evaluate our method on the 3D detection benchmark of the KITTI test server. As shown in Table 1, we compare our results with state-of-the-art RGB+Lidar and Lidar only methods for the 3D object detection and the bird’s view detection task. Our proposed method outperforms the most effective RGB+Lidar methods MMF(Liang et al. 2019) by (0.52%, 3.72%, 7.50%) for car category on three difficulty levels of 3D detection.

Compared with the Lidar-based methods, our SVGA-Net can still show decent performance on the three categories. In particular, we achieve decent results compared to Point-GNN(Shi and Rajkumar 2020) using the same graph representation method but using graph neural network in the detection of the three categories. We believe that this may benefit from our construction of local and global graphs to better capture the feature information of point clouds. The slight inferiority in the two detection tasks may be due to the fact that the local graph cannot be constructed for objects with occlusion ratio exceeding 80%.

Method	Modality	$AP_{car}(\%)$		
		Easy	Moderate	Hard
MV3D (Chen et al. 2017)	R+L	71.29	62.68	56.56
F-Pointnet (Qi et al. 2018)	R+L	83.76	70.92	63.65
AVOD-FPN (Ku et al. 2018)	R+L	84.41	74.44	68.65
F-ConvNet(Wang and Jia 2019)	R+L	89.02	78.80	77.09
Voxelnet (Zhou and Tuzel 2018)	L	81.97	65.46	62.85
SECOND (Yan, Mao, and Li 2018)	L	87.43	76.48	69.10
PointRCNN (Shi, Wang, and Li 2019)	L	88.88	78.63	77.38
Fast PointRCNN (Chen et al. 2019)	L	89.12	79.00	77.48
STD(Yang et al. 2019)	L	89.70	79.80	79.30
SA-SSD(He et al. 2020)	L	90.15	79.91	78.78
3DSSD(Yang et al. 2020)	L	89.71	79.45	78.67
Point-GNN(Shi and Rajkumar 2020)	L	87.89	78.34	77.38
SVGA-Net(ours)	L	90.59	80.23	79.15

Table 2: Performance comparison on KITTI 3D object detection val set for car class.

Performance on KITTI validation dataset. For the most important car category, we also report the performance of

Method	Modality	$AP_{car}(\%)$			$AP_{pedestrian}(\%)$			$AP_{cyclist}(\%)$		
		Easy	Moderate	Hard	Easy	Moderate	Hard	Easy	Moderate	Hard
MV3D(Chen et al. 2017)	R+L	71.09	62.35	55.12	-	-	-	-	-	-
F-Pointnet(Qi et al. 2018)	R+L	81.20	70.39	62.19	51.21	44.89	40.23	71.96	56.77	50.39
AVOD-FPN(Ku et al. 2018)	R+L	81.94	71.88	66.38	50.80	42.81	40.88	64.00	52.18	46.61
F-ConvNet(Wang and Jia 2019)	R+L	85.88	76.51	68.08	52.37	45.61	41.49	79.58	64.68	57.03
MMF(Liang et al. 2019)	R+L	86.81	76.75	68.41	-	-	-	-	-	-
Voxelnet(Zhou and Tuzel 2018)	L	77.47	65.11	57.73	39.48	33.69	31.51	61.22	48.36	44.37
SECOND(Yan, Mao, and Li 2018)	L	83.13	73.66	66.20	51.07	42.56	37.29	70.51	53.85	46.90
PointPillars(Lang et al. 2019)	L	79.05	74.99	68.30	52.08	43.43	41.49	75.78	59.07	52.92
PointRCNN(Shi, Wang, and Li 2019)	L	85.94	75.76	68.32	49.43	41.78	38.63	73.93	59.60	53.59
STD(Yang et al. 2019)	L	86.61	77.63	76.06	53.08	44.24	41.97	78.89	62.53	55.77
3DSSD(Yang et al. 2020)	L	88.36	79.57	74.55	-	-	-	-	-	-
SA-SSD(He et al. 2020)	L	88.75	79.79	74.16	-	-	-	-	-	-
PV-RCNN (Shi et al. 2020)	L	90.25	81.43	76.82	-	-	-	78.60	63.71	57.65
Point-GNN(Shi and Rajkumar 2020)	L	88.33	79.47	72.29	51.92	43.77	40.14	78.60	63.48	57.08
SVGA-Net(ours)	L	87.33	80.47	75.91	48.48	40.39	37.92	78.58	62.28	54.88

Table 1: Performance comparison on KITTI 3D object detection for car, pedestrian and cyclists. The evaluation metrics is the average precision (AP) on the official test set. 'R' denotes RGB images input and 'L' denotes Lidar point clouds input.

Difficulty	Method	3D mAP(IoU=0.7)				BEV mAP(IoU=0.7)			
		Overall	0-30m	30-50m	50m-Inf	Overall	0-30m	30-50m	50m-Inf
LEVEL_1	PointPillars(Lang et al. 2019)	56.62	81.01	51.75	27.94	75.57	92.10	74.06	55.47
	MVF(Zhou et al. 2020)	62.93	86.30	60.02	36.02	80.40	93.59	79.21	63.09
	PV-RCNN (Shi et al. 2020)	70.30	91.92	69.21	42.17	82.96	97.35	82.99	64.97
	SVGA-Net(ours)	73.45	92.53	69.44	42.08	83.52	97.60	83.14	64.25
LEVEL_2	PV-RCNN (Shi et al. 2020)	65.36	91.58	65.13	36.46	77.45	94.64	80.39	55.39
	SVGA-Net(ours)	66.65	91.65	66.78	39.29	80.97	95.54	81.58	60.18

Table 4: Performance comparison on the Waymo Open Dataset with 202 validation sequences for the vehicle detection.

Method	Modality	$AP_{car}(\%)$		
		Easy	Moderate	Hard
MV3D (Chen et al. 2017)	R+L	86.55	78.10	76.67
F-Pointnet (Qi et al. 2018)	R+L	88.16	84.02	76.44
F-ConvNet(Wang and Jia 2019)	R+L	90.23	88.79	86.84
Voxelnet (Zhou and Tuzel 2018)	L	89.60	84.81	78.57
SECOND (Yan, Mao, and Li 2018)	L	89.96	87.07	79.66
Fast PointRCNN (Chen et al. 2019)	L	90.12	88.10	86.24
STD(Yang et al. 2019)	L	90.50	88.50	88.10
Point-GNN(Shi and Rajkumar 2020)	L	89.82	88.31	87.16
SVGA-Net(ours)	L	90.27	89.16	88.11

Table 3: Performance comparison on KITTI bird's eye view detection val set for car class.

our method on KITTI val split and the results are shown in Table 2 and Table 3. For car, our proposed method achieves better or comparable results than state-of-the-art methods on three difficulty levels which illustrate the superiority of our method.

Performance on Waymo Open dataset. We evaluate our method on both LEVEL_1 and LEVEL_2 objects and compare with several top-performing methods on the Waymo Open Dataset. As shown in Table 4, with the commonly used 3D mAP evaluation metric, our method achieves new 73.45% and 83.52% mAP for the 3D object detection and bird's view detection in LEVEL_1 and outperforms PVRCNN significantly in LEVEL_2, which validates that our proposed local and global graph representations are able to effectively capture more accurate information for improving the 3D detection performance. The whole experimental re-

sults on the large-scale Waymo Open dataset further demonstrate the generalization ability of our proposed network.

Qualitative results

As shown in Figure 4, we illustrate some qualitative predicted bounding results of our proposed SVGA-Net on the test split on KITTI dataset. For better visualization, we project the 3D bounding boxes into RGB images and BEV in point clouds. From the figures we could see that our proposed network could estimate accurate 3D bounding boxes in different scenes. Surprisingly, SVGA-Net can still produce accurate 3D bounding boxes even under poor lighting conditions and severe occlusion.

Ablation studies

In this section, we conduct series of extensive ablation studies on the validation split of KITTI to illustrate the role of each module in improving the final result and our parameter selection. All ablation studies are implemented on the car class which contains the largest amount of training examples. The evaluation metric is the average precision (AP %) on the val set.

Effect of different design choice. In the local point attention layer, we stack several local complete layers to extract aggregated features. In order to show the impact of the number of the point attention layer, we train our network with n varying from 1 to 4. As shown in Table 5, when the local feature information is transmitted on the 1st to 3rd layers, the detection accuracy is continuously improved be-

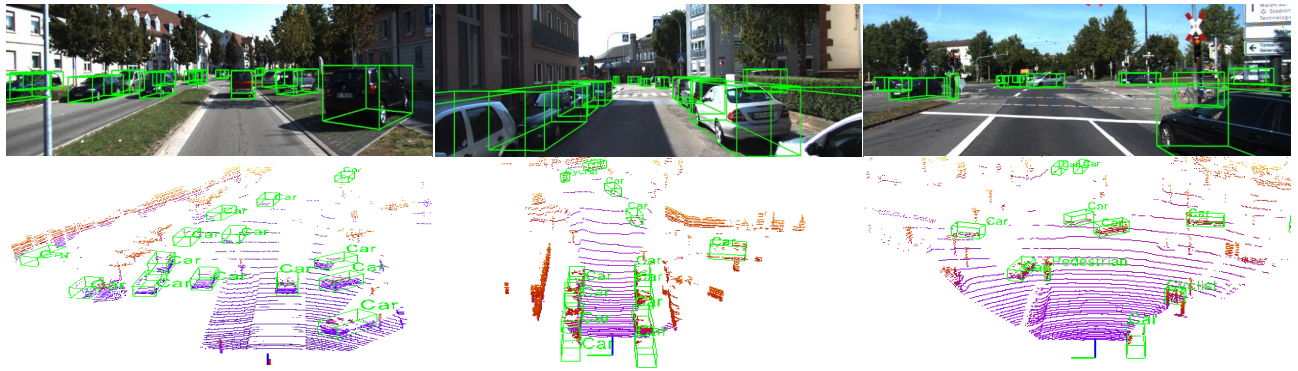


Figure 4: Qualitative 3D detection results of SVGA-Net on the KITTI test set. The detected objects are shown with green 3D bounding boxes and the relative labels. The upper row in each image is the 3D object detection result projected onto the RGB image and the bottom is the result in the corresponding point clouds.

cause the features are continuously aggregated to the object itself. When n increases to 4, the detection accuracy decreases slightly, and we believe that the network should be over-learning.

Furthermore, we study the importance of the global attention layer in improving the detection accuracy. As shown in Table 5, the AP values on both detection tasks are greatly reduced when we remove this module from the network, which proves the importance of this design in providing global feature information for each point.

		$3DAP_{car}(\%)$			$BEVAP_{car}(\%)$			
		Easy	Moderate	Hard	Easy	Moderate	Hard	
n	1	86.77	75.37	74.19	87.54	86.11	83.72	
	2	88.86	78.81	78.03	89.04	88.44	87.05	
	3	90.59	80.23	79.15	90.27	89.16	88.11	
	4	89.62	79.26	77.58	89.72	88.51	87.17	
w/o.	o.	88.42	78.11	76.54	89.71	87.45	84.33	
	w.	90.59	80.23	79.15	90.27	89.16	88.11	
		SR	87.53	77.81	76.22	86.95	86.62	85.04
		DR	88.39	78.44	76.56	87.91	86.82	86.73
		SDR	90.59	80.23	79.15	90.27	89.16	88.11
k	1	76.37	69.15	68.47	82.11	80.27	79.58	
	2	84.53	75.61	71.92	86.23	85.65	83.66	
	3	90.59	80.23	79.15	90.27	89.16	88.11	
	4	88.91	79.22	77.86	88.07	87.88	87.08	
	5	86.58	76.82	75.43	85.29	84.38	83.47	

Table 5: Performance comparison with different design choice. n is the number of point-attention layers. 'w/o.' denotes whether to keep the global attention layer. SDR denotes the sparse-to-dense regression.

In the middle three rows of Table 5, we aim to explore the effect of different design in the sparse-to-dense regression module. SR is to remove the concatenation of b_1, b_2 with the upsampled b_2, b_3 and DR is to remove the addition of b_i with F_i . Results show that only the design of sparse-to-dense regression ranks the first in improving detection accuracy.

When constructing the KNN graph, the number "3" in our implementation is chosen after series of experiments on val set, as shown in the last five rows in Table 5. When K increases from 1 to 3, the AP value has a significant increase, but when it continues to increase, the AP value does decrease.

Running time. Our network is written in Python and implemented in Pytorch for GPU computation. The average inference time for one sample is 62 ms, including 14.5%(9 ms) for data reading and pre-processing, 66.1%(41 ms) for local and global features aggregation and 19.4%(12 ms) for final boxes detection.

Conclusions

In this paper, we propose a novel sparse voxel-graph attention network(SVGA-Net) for 3D Object Detection from raw Point Clouds. We introduce graph representation to process point clouds. By constructing a local complete graph in the divided spherical voxel space, we can get a better local representation of the point feature, and the information between the point and its neighborhood can be fused. By constructing a global graph, we can better supervise and learn the features of points. In addition, the sparse-to-dense regression module can also fuse feature maps at different scales. Experiments have demonstrated the efficiency of the design choice in our network. Future work will extend SVGA-Net to combine RGB images to further improve detection accuracy.

Acknowledgments

This work is supported by a grant from the National Natural Science Foundation of China (No.61872068), by a grant from Science & Technology Department of Sichuan Province of China (No.2020YFG0037, 2020YFG0287,2021YFG0366).

References

- Bi, Y.; Chadha, A.; Abbas, A.; Bourtsoulatz, E.; and Andreopoulos, Y. 2019. Graph-Based Object Classification for Neuromorphic Vision Sensing. In *2019 IEEE/CVF International Conference on Computer Vision (ICCV)*, 491–501.
- Chen, X.; Ma, H.; Wan, J.; Li, B.; and Xia, T. 2017. Multi-view 3d object detection network for autonomous driving. In *Proceedings of the IEEE Conference on Computer Vision and Pattern Recognition*, 1907–1915.

- Chen, Y.; Liu, S.; Shen, X.; and Jia, J. 2019. Fast point r-cnn. In *Proceedings of the IEEE International Conference on Computer Vision*, 9775–9784.
- Geiger, A.; Lenz, P.; and Urtasun, R. 2012. Are we ready for autonomous driving? the kitti vision benchmark suite. In *2012 IEEE Conference on Computer Vision and Pattern Recognition*, 3354–3361. IEEE.
- Girshick, R. 2015. Fast R-CNN. In *2015 IEEE International Conference on Computer Vision (ICCV)*, 1440–1448.
- He, C.; Zeng, H.; Huang, J.; Hua, X.-S.; and Zhang, L. 2020. Structure Aware Single-stage 3D Object Detection from Point Cloud. In *Proceedings of the IEEE/CVF Conference on Computer Vision and Pattern Recognition*, 11873–11882.
- Kaul, C.; Pears, N.; and Manandhar, S. 2019. SAWSNet: A Spatially Aware Deep Neural Network for 3D Point Cloud Processing. *arXiv preprint arXiv:1905.07650*.
- Kingma, D. P.; and Ba, J. 2014. Adam: A method for stochastic optimization. *arXiv preprint arXiv:1412.6980*.
- Ku, J.; Mozifian, M.; Lee, J.; Harakeh, A.; and Waslander, S. L. 2018. Joint 3d proposal generation and object detection from view aggregation. In *2018 IEEE/RSJ International Conference on Intelligent Robots and Systems (IROS)*, 1–8. IEEE.
- Landrieu, L.; and Simonovsky, M. 2018. Large-Scale Point Cloud Semantic Segmentation with Superpoint Graphs. In *CVPR 2018*.
- Lang, A. H.; Vora, S.; Caesar, H.; Zhou, L.; Yang, J.; and Beijbom, O. 2019. PointPillars: Fast encoders for object detection from point clouds. In *Proceedings of the IEEE Conference on Computer Vision and Pattern Recognition*, 12697–12705.
- Li, B. 2017. 3d fully convolutional network for vehicle detection in point cloud. In *2017 IEEE/RSJ International Conference on Intelligent Robots and Systems (IROS)*, 1513–1518. IEEE.
- Liang, M.; Yang, B.; Chen, Y.; Hu, R.; and Urtasun, R. 2019. Multi-task multi-sensor fusion for 3d object detection. In *Proceedings of the IEEE Conference on Computer Vision and Pattern Recognition*, 7345–7353.
- Liang, M.; Yang, B.; Wang, S.; and Urtasun, R. 2018. Deep continuous fusion for multi-sensor 3d object detection. In *Proceedings of the European Conference on Computer Vision (ECCV)*, 641–656.
- Liu, Z.; Tang, H.; Lin, Y.; and Han, S. 2019. Point-Voxel CNN for efficient 3D deep learning. In *Advances in Neural Information Processing Systems*, 963–973.
- Liu, Z.; Zhao, X.; Huang, T.; Hu, R.; Zhou, Y.; and Bai, X. 2020. TANet: Robust 3D Object Detection from Point Clouds with Triple Attention. *AAAI*.
- Park, Y.; Lepetit, V.; and Woo, W. 2008. Multiple 3D Object Tracking for Augmented Reality. In *Proceedings of the 7th IEEE/ACM International Symposium on Mixed and Augmented Reality, ISMAR '08*, 117–120. Washington, DC, USA: IEEE Computer Society. ISBN 978-1-4244-2840-3.
- Qi, C. R.; Liu, W.; Wu, C.; Su, H.; and Guibas, L. J. 2018. Frustum pointnets for 3d object detection from rgb-d data. In *Proceedings of the IEEE Conference on Computer Vision and Pattern Recognition*, 918–927.
- Qi, C. R.; Su, H.; Mo, K.; and Guibas, L. J. 2017a. Pointnet: Deep learning on point sets for 3d classification and segmentation. In *Proceedings of the IEEE Conference on Computer Vision and Pattern Recognition*, 652–660.
- Qi, C. R.; Yi, L.; Su, H.; and Guibas, L. J. 2017b. Pointnet++: Deep hierarchical feature learning on point sets in a metric space. In *Advances in neural information processing systems*, 5099–5108.
- Qi, X.; Liao, R.; Jia, J.; Fidler, S.; and Urtasun, R. 2017. 3D Graph Neural Networks for RGBD Semantic Segmentation. In *2017 IEEE International Conference on Computer Vision (ICCV)*, 5209–5218.
- Redmon, J.; Divvala, S.; Girshick, R.; and Farhadi, A. 2016. You only look once: Unified, real-time object detection. In *Proceedings of the IEEE conference on computer vision and pattern recognition*, 779–788.
- Ren, S.; He, K.; Girshick, R.; and Sun, J. 2015. Faster r-cnn: Towards real-time object detection with region proposal networks. In *Advances in neural information processing systems*, 91–99.
- Shen, Y.; Feng, C.; Yang, Y.; and Tian, D. 2018. Mining Point Cloud Local Structures by Kernel Correlation and Graph Pooling. In *2018 IEEE/CVF Conference on Computer Vision and Pattern Recognition*, 4548–4557.
- Shi, S.; Guo, C.; Jiang, L.; Wang, Z.; Shi, J.; Wang, X.; and Li, H. 2020. Pv-rcnn: Point-voxel feature set abstraction for 3d object detection. In *Proceedings of the IEEE/CVF Conference on Computer Vision and Pattern Recognition*, 10529–10538.
- Shi, S.; Wang, X.; and Li, H. 2019. Pointtrcnn: 3d object proposal generation and detection from point cloud. In *Proceedings of the IEEE Conference on Computer Vision and Pattern Recognition*, 770–779.
- Shi, W.; and Rajkumar, R. R. 2020. Point-GNN: Graph Neural Network for 3D Object Detection in a Point Cloud. In *The IEEE Conference on Computer Vision and Pattern Recognition (CVPR)*.
- Simon, M.; Amende, K.; Kraus, A.; Honer, J.; Samann, T.; Kaulbersch, H.; Milz, S.; and Michael Gross, H. 2019. Complexer-yolo: Real-time 3d object detection and tracking on semantic point clouds. In *Proceedings of the IEEE Conference on Computer Vision and Pattern Recognition Workshops*, 0–0.
- Sindagi, V. A.; Zhou, Y.; and Tuzel, O. 2019. MVX-Net: Multimodal VoxelNet for 3D Object Detection. In *2019 International Conference on Robotics and Automation (ICRA)*, 7276–7282.
- Sun, P.; Kretschmar, H.; Dotiwalla, X.; Chouard, A.; Patnaik, V.; Tsui, P.; Guo, J.; Zhou, Y.; Chai, Y.; Caine, B.; et al. 2020. Scalability in perception for autonomous driving: Waymo open dataset. In *Proceedings of the IEEE/CVF Conference on Computer Vision and Pattern Recognition*, 2446–2454.

- Wang, Y.; Sun, Y.; Liu, Z.; Sarma, S. E.; Bronstein, M. M.; and Solomon, J. M. 2019. Dynamic Graph CNN for Learning on Point Clouds. *ACM Trans. Graph.*, 38(5): 146:1–146:12.
- Wang, Z.; and Jia, K. 2019. Frustum ConvNet: Sliding Frustums to Aggregate Local Point-Wise Features for Amodal. In *2019 IEEE/RSJ International Conference on Intelligent Robots and Systems (IROS)*, 1742–1749. IEEE.
- Xie, S.; Liu, S.; Chen, Z.; and Tu, Z. 2018. Attentional ShapeContextNet for Point Cloud Recognition. In *2018 IEEE/CVF Conference on Computer Vision and Pattern Recognition*, 4606–4615.
- Yan, Y.; Mao, Y.; and Li, B. 2018. Second: Sparsely embedded convolutional detection. *Sensors*, 18(10): 3337.
- Yang, B.; Luo, W.; and Urtasun, R. 2018. Pixor: Real-time 3d object detection from point clouds. In *Proceedings of the IEEE conference on Computer Vision and Pattern Recognition*, 7652–7660.
- Yang, Z.; Sun, Y.; Liu, S.; and Jia, J. 2020. 3dssd: Point-based 3d single stage object detector. In *Proceedings of the IEEE/CVF Conference on Computer Vision and Pattern Recognition*, 11040–11048.
- Yang, Z.; Sun, Y.; Liu, S.; Shen, X.; and Jia, J. 2019. Std: Sparse-to-dense 3d object detector for point cloud. In *Proceedings of the IEEE International Conference on Computer Vision*, 1951–1960.
- Yu, Y.; Huang, Z.; Li, F.; Zhang, H.; and Le, X. 2020. Point Encoder GAN: A deep learning model for 3D point cloud inpainting. *Neurocomputing*, 384: 192–199.
- Zhang, J.; Su, Q.; Wang, C.; and Gu, H. 2020. Monocular 3D Vehicle Detection with Multi-instance Depth and Geometry Reasoning for Autonomous Driving. *Neurocomputing*.
- Zhou, Y.; Sun, P.; Zhang, Y.; Anguelov, D.; Gao, J.; Ouyang, T.; Guo, J.; Ngiam, J.; and Vasudevan, V. 2020. End-to-end multi-view fusion for 3d object detection in lidar point clouds. In *Conference on Robot Learning*, 923–932. PMLR.
- Zhou, Y.; and Tuzel, O. 2018. Voxelnet: End-to-end learning for point cloud based 3d object detection. In *Proceedings of the IEEE Conference on Computer Vision and Pattern Recognition*, 4490–4499.